RSC Advances

PAPER

View Article Online
View Journal | View Issue

Cite this: *RSC Adv.*, 2017, **7**, 4078

Microemulsion prepared $Ni_{88}Pt_{12}$ for methane cracking†

Lu Zhou,*[ab] Moussab Harb,[b] Mohamed Nejib Hedhili,[c] Noor Al Mana[b] and Jean Marie Basset*[b]

Received 11th October 2016
Accepted 17th November 2016

DOI: 10.1039/c6ra25069f

www.rsc.org/advances

Monodispersed $Ni_{88}Pt_{12}$ nanoparticles of 10 nm were synthesized by water-in-oil microemulsion. The Ni–Pt alloy structure was stable during the thermal treatment between 330 and 1037 °C, whereas the relatively low temperature range of 600–700 °C was favorable for methane cracking to produce hydrogen and carbon nanotubes.

The methane cracking process has been extensively studied over the last few decades to simultaneously produce CO/CO_2-free hydrogen and high value added carbon by-products.[1–3] It is reported that, in the case of >50% methane conversion, methane cracking would be competitive against commercial methane steam reforming, but with a 20% lower carbon footprint.[4] However, the realization of a continuous methane cracking process over catalysts with good activity and stability can be hampered by reactor plugging and/or pressure drops associated with the substantial carbon formation; thus, fluidized bed reactors have been proposed as a solution to these challenges.[5] In existing reports,[6–8] Ni-based catalysts are recognized to be the most reactive, and many researchers are studying them for methane cracking at 500–900 °C to produce H_2 and carbon nanomaterials, including multiple wall carbon nanotubes (MWCNT) and/or carbon nano-onions (CNO). However, as represented in Table 1, there is still no agreement on the relationship between reaction condition, carbon morphology and catalyst activity, mainly due to differences in catalyst composition (supports and/or Ni loading and/or additives).

In recent years, much attention has been focused on the development of unsupported Ni-based catalysts to avoid the formation of CO_x during the reaction between CH_4 and lattice oxygen in the supports. By precipitation of nickel acetate and sodium carbonate aqueous solution with the mediation of ethylene glycol, Y. Li *et al.*[14] developed a novel bulk Ni catalyst showing a stable methane cracking activity at 500 °C for as long as 50 h. A Ni–Cu–Co alloy catalyst, prepared by the thermal decomposition of the oxalate precursors, also showed good catalytic activity for methane cracking in the temperature range from 650 to 775 °C.[9] In our study, an unsupported Ni–Pt alloy, $Ni_{88}Pt_{12}$, was prepared by a water-in-oil (W/O) microemulsion method. Compared to the monometallic Ni and Pt catalysts, the Ni–Pt alloy catalyst exhibited superior activity for methane cracking. We further investigated the influence of reaction temperature and space velocity on the catalytic activity and deposited carbon morphology, with the aim of optimizing the reaction conditions to maintain the activity and stability of the catalyst.

$Ni_{88}Pt_{12}$ was prepared by reduction with hydrazine of $Ni(NO_3)_2$ mixed with $PtCl_4$ in a W/O microemulsion, formed by the nonionic surfactant Triton X-100, cyclohexane and water (Fig. 1a; see ESI†). Fig. 1b presents the typical high-resolution transmission electron microscopy (HRTEM) image together with the size distribution of the as-synthesized products. It was evident that spherical nanoparticles of *ca.* 10 nm were monodispersed throughout the $Ni_{88}Pt_{12}$ sample. The existence of both Ni and Pt over one selected particle was clearly indicated in the energy-dispersive X-ray (EDX) spectrum shown in Fig. 1c. The crystallinity characteristics of $Ni_{88}Pt_{12}$ were further investigated by the X-ray diffraction (XRD) pattern (Fig. 1d), in which the diffraction peaks were indexed and ascribed to the (111), (200) and (220) reflections of face centred cubic (fcc) Ni–Pt alloy (JCPDS no. 65-2797).[15] The chemical state of $Ni_{88}Pt_{12}$ was examined by X-ray photoelectron spectroscopy (XPS), as shown in Fig. 1e. Deconvolution of Pt 4f and Ni 2p XPS profiles indicated the coexistence of both Pt^0 and Ni^0 metals as the major components on the surface of $Ni_{88}Pt_{12}$. The Ni 2p spectrum was complicated by the presence of a high binding energy satellite peak (861.7 eV) adjacent to the main peaks. The two peaks centering at 852.5 and 855.5 eV were assigned to Ni^0 and Ni^{2+}, respectively. Minor formation of oxidized Ni^{2+} may have been caused during the sample preparation for the XPS measurements.[16] The Pt 4f core level was fitted using two doublets

[a]*Key Laboratory of Flexible Electronics (KLOFE), Institute of Advanced Materials (IAM), Jiangsu National Synergetic Innovation Center for Advanced Materials (SICAM), Nanjing Tech University (NanjingTech), 30 South Puzhu Road, Nanjing 211816, China. E-mail: iamlvzhou@njtech.edu.cn*

[b]*KAUST Catalysis Center, King Abdullah University of Science and Technology, Thuwal 23955-6900, Saudi Arabia. E-mail: jeanmarie.basset@kaust.edu.sa*

[c]*Core Lab, King Abdullah University of Science and Technology, Thuwal 23955-6900, Saudi Arabia*

† Electronic supplementary information (ESI) available: Experimental details, computation method. See DOI: 10.1039/c6ra25069f

Table 1 Review of methane cracking over Ni-based catalysts

Catalyst	Reaction condition		H_2 formation[b] L g_{cat}^{-1} h^{-1}	Carbon
	°C	L g_{cat}^{-1} h^{-1}[a]		
$Ni_{0.7}Cu_{0.05}Co_{0.25}$ (ref. 9)	750	6	4.8	MWCNT + CNO
13Ni@C-B_2O_3 (ref. 10)	850	3	10.2	CNO
50%Ni/SiO_2 (ref. 11)	800	5	4.4	MWCNT
12%Ni/TiO_2 (ref. 12)	500	9	3.24	MWCNT
NiO[13]	900	38	16	CNO

[a] Space velocity. [b] After 30 min reaction.

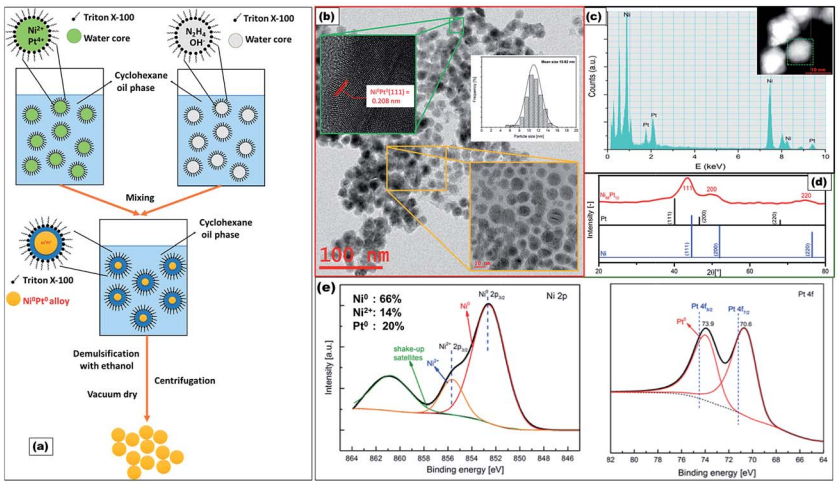

Fig. 1 (a) Schematic for the one-pot synthesis of $Ni_{88}Pt_{12}$; (b) HRTEM of fresh $Ni_{88}Pt_{12}$; (c) EDX spectra of one selected $Ni_{88}Pt_{12}$ particle; (d) XRD pattern over fresh $Ni_{88}Pt_{12}$; (e) XPS spectrum of Pt 4f, Ni 2p regions of fresh $Ni_{88}Pt_{12}$.

Pt $4f_{7/2}$–Pt $4f_{5/2}$ with a fixed area ratio equal to 4 : 3 and doublet separation of 3.3 eV. The negative shift of the 4f peaks (about 0.6 eV compared to pure Pt metal, vertical lines) should be attributed to the alloying of Pt with Ni atoms, which agrees well with the XRD results.

For comparison, monometallic Ni and Pt samples, named as ME-Ni and ME-Pt. Were also synthesized using the microemulsion method, as described in the ESI.† As indicated by Fig. 2a, adding 31 wt% Pt into ME-Ni catalyst dramatically improves its activity. Methane cracking activity on the transition metals is related to their d-electron configuration. Ni is well known to show much better methane cracking activity than Pt. As suggested by XPS analysis, considering that the much higher concentration of Ni than that of Pt, the presence Ni–Pt alloy may electronically and geometrically modify the Ni^0 surface structure, which in turn may have an influence on the catalytic performance. It was probable that the formation of the Ni–Pt alloy tuned the d-electron structure, thus favoring CH_4 activation–decomposition on ME-$Ni_{88}Pt_{12}$. The effect of the Pt/Ni ratio

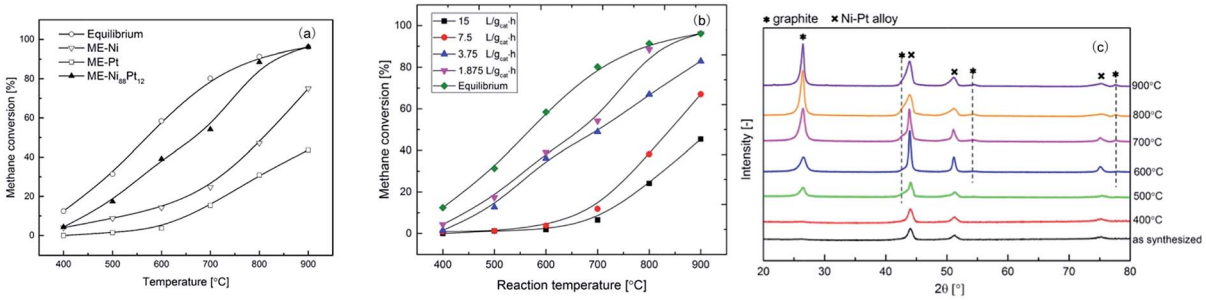

Fig. 2 (a) Activity comparison over microemulsion prepared samples at SV = 1.875 L g_{cat}^{-1} h^{-1}; (b) the activity of $Ni_{88}Pt_{12}$ for methane cracking; (c) *in situ* XRD pattern on $Ni_{88}Pt_{12}$ during methane cracking at 400–900 °C under SV = 1.875 L g_{cat}^{-1} h^{-1}.

on the catalytic activity of the alloy is under study and will be reported later.

The influence of SV on the initial methane cracking activity of $Ni_{88}Pt_{12}$ was further studied, as shown in Fig. 2b, over an SV range of 1.875 to 15 L g_{cat}^{-1} h^{-1}. Clearly, by prolonging the contact time between methane and the catalyst surface, a high initial methane conversion could be achieved at all temperatures ranging from 400–900 °C. Under a low SV of 1.875 L g_{cat}^{-1} h^{-1}, $Ni_{88}Pt_{12}$ methane conversion at 800–900 °C almost exhibited an equilibrium value. Regardless of SV, all samples in Fig. 2b showed incremental changes in methane conversion with increase in temperature over a range from 400 to 900 °C. As methane cracking is a moderate endothermic reaction, it was obvious that higher temperatures favored the methane cracking. The gradual strengthening of the graphite diffraction peaks with temperature during methane cracking over $Ni_{88}Pt_{12}$ was monitored *in situ* by XRD, as shown in Fig. 2c; it further indicated that high temperature stimulated the methane cracking and accelerated the simultaneous carbon deposition over the catalyst. On the other hand, the structure of the Ni–Pt alloy was retained, although the aggregation of Ni–Pt particles may have probably resulted in the sharpness of the reflection peaks with increase in temperature.

A further study of $Ni_{88}Pt_{12}$ structure change with temperature was conducted by density functional theory (DFT) computations (see ESI†). Fig. 3 displays the key explored DFT-optimized atomic configurations for the Ni–Pt 55-atom icosahedron, $Ni_{48}Pt_7$ nanocluster (Ni/Pt ratio very close to the experimental $Ni_{88}Pt_{12}$), generated from a direct substitution of 7 neutral Ni atoms by 7 neutral Pt atoms at different occupation sites, including core–shell and random alloy dispositions. For each structural configuration, the relative energy was computed (given in brackets) to determine the most stable configuration at room temperature and the structure evolution as a function of treatment temperature to understand the obtained experimental structure of the bimetallic Ni–Pt nanoparticles prepared in this study. The lowest-energy structure was obtained when all Pt atoms are well dispersed on the surface without any Pt–Pt bonding, as shown in Fig. 3A, with computed surface Ni–Pt bond lengths ranging from 2.53 to 2.56 Å. This indicated that this geometrical configuration was likely to be the most energetically favorable at room temperature. However, the configuration displaying a complete Pt segregation on the surface with a maximal number of Pt–Pt bonds and computed surface Ni–Pt bond lengths ranging from 2.47 to 2.63 Å and Pt–Pt bond lengths ranging from 2.70 to 2.82 Å, was found to be less stable by 32 meV per atom than the one abovementioned (Fig. 3B). Interestingly, the structural configuration showing a random alloy composition (4 well-dispersed Pt atoms on the surface and 3 well-dispersed Pt atoms in the core without any Pt–Pt bonding), with computed surface Ni–Pt bond lengths ranging from 2.55 to 2.57 Å, was found to be less favorable than the first one by 52 meV per atom (Fig. 3C). As a typical estimate, the fully segregated Pt and random distribution structures became significant around 100 and 330 °C, respectively. Indeed, incorporating more Pt atoms into the core of the nanoparticle led to higher relative electronic energies with respect to that in the previous case. The configurations with 1, 2 and 3 additional Pt atoms incorporated into the core forming, 1, 3 and 4 new Pt–Pt bonds and computed surface Ni–Pt bond lengths of 2.55 to 2.58 Å, were found to be 71, 92 and 113 meV per atom less stable, respectively, than the first one (Fig. 3D–F). As a consequence, these structural dispositions became significant around 550, 794 and 1037 °C, respectively. Clearly, although more Pt atoms were incorporated into the core of the Ni nanoparticles at higher temperatures, forming more Pt–Pt bonds, the remaining alloy structure of Ni–Pt can still be confirmed by the DFT study over the temperature range from 400 to 900 °C, corresponding to the XRD results presented in Fig. 2. The DFT results also suggested that for $Ni_{88}Pt_{12}$ under thermal treatment lower than 330 °C, the Pt phase was dominant on the sample surface compared to the Ni phase. This provided a satisfactory explanation for the higher Pt/Ni molar ratio (20/80) calculated by the XPS analysis (Fig. 1E) as compared to the ratio determined by elemental analysis (12/88), as the XPS value can only represent the state of the sample surface of 3–10 nm in depth. Higher ratio of Pt/Ni at the surface than in the bulk material was also reported by K. W. Park *et al.*,[17] who found that the ratio of surface Pt/Ni analyzed by XPS changed from 9/1 at room temperature to 7/3 at 300 °C and 2/8 at 500 °C.

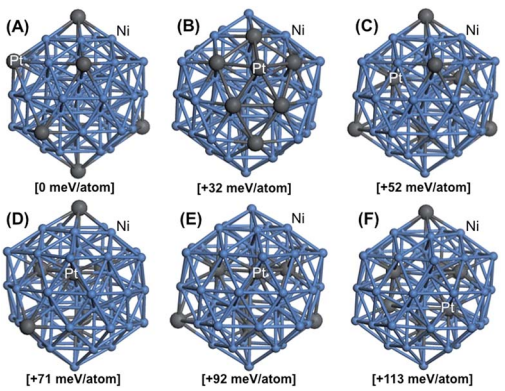

Fig. 3 DFT-optimized structural isomers for the Ni–Pt 55-atom icosahedron $Ni_{48}Pt_7$ nanocluster. Color legend: Ni atoms are shown in light blue and Pt atoms in dark gray.

The stability of $Ni_{88}Pt_{12}$ during methane cracking under a low SV of 1.875 L g_{cat}^{-1} h^{-1} was investigated at different temperatures in the range of 600–900 °C, as illustrated in Fig. 4a. After 300 min, severe catalyst deactivations in terms of methane conversion loss of *ca.* 50% and 80% was observed for the samples tested at 800 and 900 °C, respectively. On the other hand, for the lower temperature methane cracking (600 and 700 °C), $Ni_{88}Pt_{12}$ exhibited a relatively more stable activity. Less than 10% deactivation was observed for the sample tested at 700 °C, whereas negligible deactivation was detected at 600 °C. Obviously, as the temperature increased, the initial catalytic activity was improved; however, deactivation occurred more rapidly. Carbon deposition over the sample surface to cover the active sites is always reported to be the main reason for catalyst deactivation during methane cracking. Massive deposition of carbon on all spent samples after life test was observed by

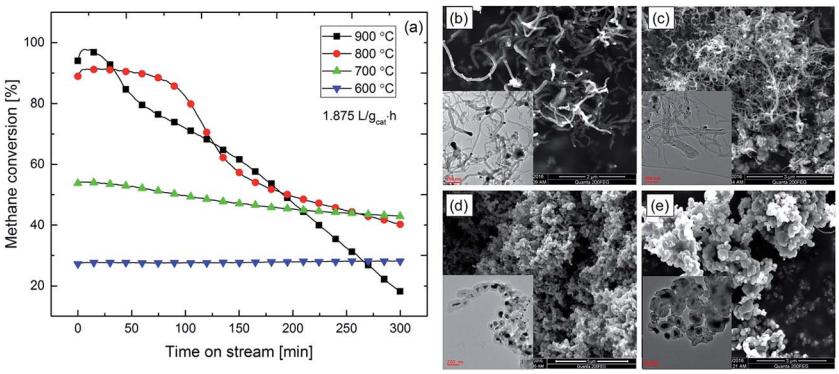

Fig. 4 (a) Life test of $Ni_{88}Pt_{12}$ at different temperature under SV = 1.875 L g_{cat}^{-1} h^{-1}; surface morphology over samples after lift test at (b) 600 °C; (c) 700 °C; (d) 800 °C; and (e) 900 °C.

electron microscopy (Fig. 4b–e). After reaction at low temperatures of 600 °C (Fig. 4b) and 700 °C (Fig. 4c), MWCNTs were preferentially formed, whilst CNOs formation were favored at higher cracking temperatures of 800 °C (Fig. 4d) and 900 °C (Fig. 4e). It should be noted that metallic Ni–Pt alloy particles were found to be dispersed and anchored on the tip of formed MWCNTs. These anchored particles could be still available to act as catalysts for methane cracking. However, Ni–Pt metal particles encapsulated by a thick layer of graphite were absolutely inactivated. According to thermal gravimetric analysis (TGA), samples after reaction at 900 and 700 °C had similar carbon deposition amounts of 2.9 and 2.7 g_c g_{cat}^{-1}, respectively. Considering the catalyst deactivation behavior, together with carbon deposition amount and morphologies, it can be speculated that deactivation was more strongly influenced by the carbon growth mechanism rather than the amount deposited on the sample.

As reported in our previous studies,[5,18,19] the carbon growth mechanism was totally different between Ni and Fe-based catalysts. It is widely accepted that, during Fe-catalyzed methane cracking, graphite originates from the decomposition of an intermediate phase Fe_3C,[20] whereas carbon is believed to diffuse through the bulk of Ni particles, and then precipitate as graphite on the Ni (111) surface.[5]

During Ni-catalyzed methane cracking, four main steps are assumed to occur: (i) CH_4 bond activation, followed by further decomposition on the Ni particle to produce H_2 and carbon, (ii) atomic carbon diffusion through the bulk of the Ni particles, (iii) surface diffusion of C to specific planes of Ni, and (iv) carbon–carbon bond formation, leading either to CNT or CNO. The $Ni_{88}Pt_{12}$ structure is maintained in the temperature range of 600–900 °C, as evidenced by the XRD and DFT results (discussed in Fig. 2 and 3). This shows that the morphology of the deposited carbon is not controlled by the crystalline structure of the catalyst; in this range of temperature, the morphology of the carbon is changing from CNT to CNO, whereas the morphology and structure of the catalyst is thermally stable. It is therefore reasonable to propose that the carbon morphology over $Ni_{88}Pt_{12}$ catalyst is defined by the respective rates of step (i) and steps (ii) and (iii), which are temperature dependent. At high temperature, methane cracking to "chemisorbed" carbon is reasonably assumed to proceed with a much higher rate than that of diffusion in the bulk. Because carbon diffusion in the bulk is becoming rate determining, another pathway prevails; that is, the fast migration of "chemisorbed" carbon around the particle leading to CNO. On the other hand, at low temperature, when the rate of carbon formation (step (i)), diffusion in the bulk (step (ii)) and graphite formation (step (iv)) can achieve an equilibrium state, carbon would be smoothly diffused through the core of Ni and thus formation of CNTs anchored to metal nanoparticles on the tip would be favored.

In summary, a W/O microemulsion method was used to synthesize bulk Ni–Pt bimetallic catalysts, which were studied for methane cracking. The influence of the reaction conditions on the catalyst's activity and carbon deposition morphology were investigated with both experimental and computational methods. The formation of metallic Ni–Pt alloy structure over $Ni_{88}Pt_{12}$ is evidenced by XRD, TEM and XPS. This structure can be retained over temperature range of 330–1037 °C according to DFT study. Although high initial activity can be achieved at high temperature of 800–900 °C, catalyst deactivation was severe due to the total encapsulation of the active metals by a thick graphite layer (CNO). CNTs anchoring metallic Ni–Pt alloy particles were observed on $Ni_{88}Pt_{12}$ during methane cracking at a lower temperature of 600–700 °C. Because the mechanism does not involve surface migration but bulk diffusion, the catalyst did not deactivate with time. The methodology and results reported here maybe useful for designing methane cracking reactors based on Ni catalysts to produce hydrogen and carbon nanomaterials.

Acknowledgements

We thank KAUST and the National Natural Science Foundation of China (21403108) for the financial support.

Notes and references

1 D. Ping, C. X. Wang, X. F. Dong and Y. C. Dong, *Appl. Surf. Sci.*, 2016, **369**, 299–307.
2 T. Maneerung, K. Hidajat and S. Kawi, *Int. J. Hydrogen Energy*, 2015, **40**, 13399–13411.

3 X. X. Li, G. L. Zhu, S. T. Qi, J. Huang and B. L. Yang, *Appl. Energy*, 2014, **130**, 846–852.
4 K. C. Mondal and S. R. Chandran, *Int. J. Hydrogen Energy*, 2014, **39**, 9670–9674.
5 L. Zhou, Y. Guo and K. Hideo, *AIChE J.*, 2014, **60**, 2907–2917.
6 N. Bayat, M. Rezaei and F. Meshkani, *Int. J. Hydrogen Energy*, 2016, **41**, 5494–5503.
7 N. Bayat, M. Rezaei and F. Meshkani, *Int. J. Hydrogen Energy*, 2016, **41**, 1574–1584.
8 M. Pudukudy, Z. Yaakob and M. S. Takriff, *Appl. Surf. Sci.*, 2015, **356**, 1320–1326.
9 A. C. Lua and H. Y. Wang, *Appl. Catal., B*, 2014, **156**, 84–93.
10 D. Kang and J. W. Lee, *Appl. Catal., B*, 2016, **186**, 41–55.
11 M. Pudukudy and Z. Yaakob, *Chem. Eng. J.*, 2015, **262**, 1009–1021.
12 Y. Shen and A. C. Lua, *J. Power Sources*, 2015, **280**, 467–475.
13 U. P. M. Ashik and W. M. A. W. Daud, *J. Taiwan Inst. Chem. Eng.*, 2016, **61**, 247–260.
14 Y. Li, B. C. Zhang, X. W. Xie, J. L. Liu, Y. D. Xu and W. J. Shen, *J. Catal.*, 2006, **238**, 412–424.
15 L. L. Zou, J. Fan, Y. Zhou, C. M. Wang, J. Li, Z. Q. Zou and H. Yang, *Nano Res.*, 2015, **8**, 2777–2788.
16 L. Wen, X. Q. Du, J. Su, W. Luo, P. Cai and G. Z. Cheng, *Dalton Trans.*, 2015, **44**, 6212–6218.
17 K. W. Park, J. H. Choi and Y. E. Sung, *J. Phys. Chem. B*, 2003, **107**, 5851–5856.
18 L. Zhou, L. R. Enakonda, Y. Saih, S. Loptain, D. Gary, P. Del-Gallo and J. M. Basset, *ChemSusChem*, 2016, **9**, 1243–1248.
19 L. Reddy Enakonda, L. Zhou, Y. Saih, S. Ould-Chikh, S. Lopatin, D. Gary, P. Del-Gallo and J.-M. Basset, *ChemSusChem*, 2016, **9**, 1911–1915.
20 A. K. Schaper, H. Q. Hou, A. Greiner and F. Phillipp, *J. Catal.*, 2004, **222**, 250–254.